Lawrence Berkeley National Laboratory

Title

The Effect of the SEI Layer Mechanical Deformation on the Passivity of a Si Anode in Organic Carbonate Electrolytes

Permalink

https://escholarship.org/uc/item/97s5c9xk

Authors

Yoon, Insun

Larson, Jonathan M

Kostecki, Robert

The Effect of the SEI Layer Mechanical Deformation on the Passivity of a Si Anode in Organic Carbonate Electrolytes

Insun Yoon[‡], Jonathan M. Larson[‡], Robert Kostecki[*]

Energy Storage and Distributed Resources Division, Lawrence Berkeley National Laboratory, Berkeley, CA 94720 USA

[‡]Equally contributing authors

[*]Corresponding author; E-mail: r_kostecki@lbl.gov

ABSTRACT

The solid electrolyte interphase (SEI) on a Si negative electrode in carbonate-based organic electrolytes shows intrinsically poor passivating behavior, giving rise to unsatisfactory calendar life of Li-ion batteries. Moreover, mechanical strains induced in the SEI due to large volume changes of Si during charge-discharge cycling could contribute to its mechanical instability and poor passivating behavior. This study elucidates the influence of static mechanical deformation of the SEI has on the rate of unwanted parasitic reactions at the Si-electrolyte interface as a function of electrode potential. The experimental approach involves the utilization of Si thin-film electrodes on substrates with disparate elastic moduli, which either permit or suppress the SEI deformation in response to Si volume changes upon charging-discharging. We find that static mechanical stretching and deformation of the SEI results in an increased parasitic electrolyte reduction current on Si. Furthermore, attenuated total reflection and near-field Fourier-transform infrared nanospectroscopy reveal that the static mechanical stretching and deformation of the SEI fosters a selective transport of linear carbonate solvent through, and nanoconfinement within, the SEI. These, in turn, promote selective solvent reduction and continuous electrolyte decomposition on Si electrodes, reducing the calendar life of Si anode-based Li-ion batteries. Finally, possible correlations between the structure and chemical composition of the SEI layer and its mechanical and chemical resilience under prolonged mechanical deformation are discussed in detail.
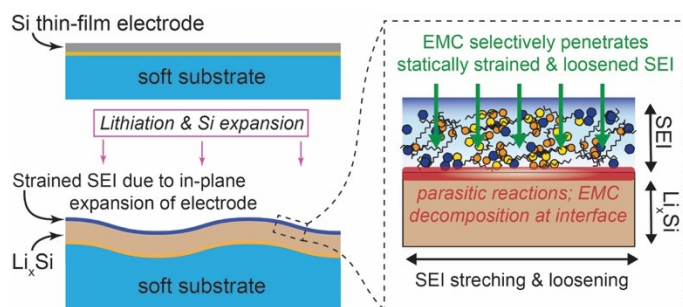
30

31

32

33

34

35 **TOC FIGURE**

36   The Si negative electrode has nearly an order of magnitude higher specific energy density than graphite

37   Li-ion anodes (3579 mAh/g vs. 372 mAh/g).[1] However, electrochemical cycling of Si is accompanied by

38   large volume changes (~300% when fully lithiated)[2,3] that give rise to various degradation mechanisms

39   such as Si particle fracture and/or composite electrode delamination, which facilitate rapid capacity fade[4].

40   Recent advances in nanoscale Si (nanoparticles or nanowires) synthesis and composite electrode

41   assembly/architecture have helped to manage stress accumulation and mitigate Si intra/interparticle

42   fracture issues.[2,5,6] As a result, state-of-the-art Si-based anodes have shown much improved cycle life,[7-10]

43   and therefore cycle life related issues are not the subject of this study.

44

45   Another challenge that lithium-ion batteries (LIBs) utilizing Si anodes face is that of subpar calendar life.

46   The primary contributor to this is the Si anode's intrinsic non-passivating behavior in carbonate-based

47   electrolytes.[11,12] This is attributed to the nonideality of the SEI layer: a few tens of nanometers thin layer

48   of electrolyte reduction products deposited at the Si/electrolyte interface. Upon formation, an ideal SEI

49   should fully passivate the electrode surface, inhibiting any unfavorable side reactions at the interface.

50   Failure to do so results in the continuous consumption of electrolyte and cyclable lithium, compromising

51   long-term cell stability.[13,14] Thus, the quality and integrity of the SEI are widely considered to be critical

52   factors in determining the overall performance of LIBs.[15] Unfortunately, the SEI layer that forms on the

53   Si surface is constantly evolving[11,16] and plagued with parasitic side reactions at rates *ca.* 10x higher than

54   at graphite anodes;[17] leading to poor calendar life, despite sufficient cycle life.

55

56   Another contributor to the aforementioned non-passivating behavior of Si may originate from mechanical

57   instability of the already imperfect SEI. Upon large Si volume changes the SEI can realize substantial

58 mechanical deformations which can contribute to the poor passivation behavior. Generally, mechanical

59 instability of the SEI contributes to Si electrode failure mechanisms in at least two of the following ways:

60 (i) explicit mechanical failures such as SEI cracking or delamination (which is typically followed by

61 subsequent reformation of SEI on exposed areas of the Si surface), or (ii) implicit mechanical failure and

62 interfacial instability due to structural and morphological changes in the SEI in response to stress. The

63 explicit mechanical failure mechanism happens when Si is undergoing continuous volume changes during

64 electrochemical charge-discharge cycling. Thus, this failure mode is most relevant to cycle life, and has

65 been extensively investigated both experimentally and theoretically,[18-21] and is not the subject of this

66 study. On the other hand, the implicit mechanical failure can happen even when the cell is at rest. To

67 elaborate, one must realize that the SEI layer operates under various, and even severe, static strains,

68 depending on the state of charge of the Si electrode. With the alleged inhomogeneous structure and high

69 porosity of the SEI,[22-24] severe stretching or contracting forces may compromise the SEI's passivating

70 properties. Therefore, this failure mechanism (implicit mechanical failure), in addition to the inherent

71 non-passivating behavior of the film, can be particularly relevant to Si-based LIB calendar life.

72

73 Typically, the interfacial behavior of Si is investigated either in a model thin-film or composite electrode

74 configuration. While the former is suitable for an accurate evaluation of parasitic current per unit area and

75 relevant *in situ* or post-mortem surface analyses, in-plane expansion of the Si thin-film and associated

76 mechanical deformation of SEI are typically entirely restricted by relatively thick and stiff current

77 collectors, such as battery-grade Cu foil. Thus, these experimental approaches cannot probe the influence

78 that static strains may have on SEI passivation stability. In the case of the Si composite electrode system,

79 the volume change of active materials is comparably unrestricted, but the mechanical strain may be

80 unevenly distributed across the bulk of the electrode. Moreover, the overall parasitic current is a

81 convolution of contributions from both active and passive electrode components, which impedes accurate

82 surface characterization. Therefore, distinguishing between cathodic currents originating from the

83 imperfect passive film (SEI) on the Si surface versus those specifically associated with static strain in SEI

84 is nearly impossible. For these reasons, a custom-designed experimental platform is needed to measure

85 and assess the impact that static mechanical strain has on the SEI film passivation behavior.

86

87 In this study, we carried out an investigation aimed at understanding what influence static SEI mechanical

88 strain has on passivation stability of Si electrodes. This was undertaken with a comparative experimental

89 approach between two model Si electrodes prepared on substrates with dissimilar elastic properties. One

90 allowed in-plane expansion and mechanical deformation of the SEI while the other restricted in-plane

91 expansion, and inhibited SEI deformation. The samples were subjected to electrochemical testing and *ex*

92 *situ* surface chemistry analyses. These revealed an unambiguous influence that static mechanical

93 deformation of the SEI layer has on the magnitude of the parasitic electrolyte reduction current, and the

94 chemical composition of the SEI.

95

96 **RESULTS AND DISCUSSION**

97 ***Fabrication of model Si electrodes that realize disparate amounts of strain upon lithiation.*** Two types

98 of electrode substrate materials were adopted for this comparative study: polydimethylsiloxane (PDMS)

99 and fused silica. Both materials are inert to lithium-ion battery chemistry and do not affect corresponding

100 electrochemical processes.[25] PDMS mono/dimers were mixed with a crosslinker in a ratio of 10:1 and

101 drop-casted on a 25 mm diameter fused silica disc (which served as a handling substrate) and was cured at

102 70°C for three hours. The surfaces of both the fused silica/PDMS and bare fused silica substrates (we call

103 them soft and rigid substrates herein, respectively) were then subjected to oxygen plasma treatment prior

104   to sputter deposition of the Ti/Ni/Si layers, which were 5, 40, and 50 nm in thickness, respectively (see

105   Methods for complete details). A schematic depiction of the sample electrode structures is illustrated in

106   Figure 1a.

107

108   In principle, electrochemical cycling of amorphous Si should induce isotropic volume changes. However,

109   when a thin-film is coated onto another material, the underlying substrate's rigidity significantly

110   influences the in-plane expansion and contraction of the amorphous Si. In the case of the rigid fused silica

111   substrate (Young's modulus ~72 GPa),[26] in-plane expansion upon lithiation was entirely restricted, and

112   only out-of-plane expansion proceeded.[27] On the other hand, the soft PDMS substrate (Young's modulus

113   ~2 Mpa)[28] allowed both out-of-plane and some degree of in-plane expansion.[29] The combination of in-

114   and out-of-plane expansion of the Si film on the soft substrate leads to the formation of surface wrinkles

115   (Figure 1b).[30] These shape changes could be controlled as a function of the electrode state-of-charge

116   (SOC) and are direct evidence of expansion and deformation of the Si film and associated mechanical

117   strain induced in the SEI. In the case of the rigid fused silica substrate, the SEI on Si tends to remain

118   undeformed. This comparative approach offered a pathway to extract and elucidate the influence that SEI

119   deformation had on the electrochemical response. For the sake of clarity and brevity, we name the soft

120   PDMS substrate case 'SEI deformed' and the rigid fused silica substrate case 'SEI undeformed'.

121

Figure 1. (a) Cross-sectional illustration of (i) soft (PDMS) and (ii) rigid (fused silica) substrate samples. Ic

122

Custom electrochemical cell designs and assembly. Custom electrochemical cells were designed and
fabricated to accommodate the geometry of the Si electrodes and prevent side reactions that could be
attributable to cell materials during cycling (see schematics presented in supporting information section
S1). The cells were made of polyether ether ketone (PEEK), which possess the requisite chemical
compatibility with the Li-ion electrolyte solvents and salts.[31,32] A primary cell configuration (Figure S1a)
was utilized in all electrochemical measurements herein except for the *in situ* optical microscopy to be
described in detail later. In this primary cell configuration, the working electrode was located at the cell
base and a Li foil disc was attached to the cell cover, adjacent to the Si electrode in a co-facial
arrangement. The Li foil served as the counter and reference electrode and the two electrodes were
physically separated by an ~700 μm gap of electrolyte.

134 In a modified cell version (Figure S1b), a fused silica optical window was positioned in a co-facial

135 arrangement, adjacent to the Si working electrode, rather than Li. This was done to allow light passage

136 for the observation of electrode surface evolution using *in situ* optical microscopy. This modified cell

137 with Li counter electrode laterally offset from the Si working electrode would likely experience

138 overpotentials. We stress this cell was not utilized for parasitic current measurements and associated *ex*

139 *situ* strain, topographic, and spectroscopic surface characterizations. All those utilized the primary cell

140 described in the previous paragraph and all potentials refer to Li/Li$^+$ electrode. Further technical details

141 about the electrochemical cell can be found in the Methods section and Supporting Information.

142

143 ***Electrochemical protocols for measuring passivation stability via steady-state parasitic current density.***

144 The Si electrode passivation stability was quantified by measuring a steady-state parasitic current density

145 during long-term (12 hr) potentiostatic polarization at various SOCs. A similar approach has been applied

146 to composite-type electrodes.[17,33] First, the Si electrode underwent three voltametric (CV) formation

147 cycles at a sweep rate of 0.1 mV/s between 1.5 – 0.05 V. Subsequently, linear potential sweeps at a scan

148 rate of 0.1 mV/s between 1.5 – 0.05 V were carried out with 12-hour-long potentiostatic holds at 0.7, 0.5,

149 0.3, 0.1 and 0.05 V during the cathodic and 0.1, 0.3, 0.5, 0.7, 1.5 V during the anodic sweep. The

150 parasitic current was recorded at the end of each potentiostatic hold where reversible reaction is

151 negligibly small and parasitic reaction is dominant. These measurements were repeated during two full

152 cycles to observe the parasitic current evolution. While explicit mechanical failures due to Si volume

153 changes and Si/SEI cracking were also expected, the potential was held sufficiently long (12 hours) to

154 allow the SEI layer to reform on any exposed Si surfaces. Therefore, any discrepancy in the parasitic

155   current between the 'SEI deformed' and 'SEI undeformed' electrodes was attributed to affects associated

156   with static mechanical strain applied to the SEI.

157

158   ***SEI/Si strain measurements via optical microscopy and white light interferometry.***   Two optical

159   techniques were utilized to observe strain: simple *in situ* optical microscopy and *ex situ* white light

160   interferometry (WLI). The former is ideal at qualitatively imaging reversible strain during cycling, while

161   the latter is ideal at quantifying strain amounts at specific potentials. We note both kinds of strain

162   measurements were only collected on the SEI deformed electrodes. This is because it is already known in

163   the literature[27] that there will be negligibly small in plane strain and associated surface area change in the

164   SEI undeformed electrodes where the rigid fused silica substrate restricts in plane expansion of the Si

165   electrode. On the other hand, in the case of the SEI deformed electrode, during lithiation, in-plane

166   expansion of the electrode is expected because of the compliance of the PDMS substrate. Thus, we

167   measured SEI deformation and strain in the SEI deformed case, as a function of electrode potential and

168   SOC. Furthermore, as will be shown in detail later, the expansion at times was large enough to induce

169   buckling instabilities[29] which resulted in the formation of surface wrinkles in the Si thin film electrode

170   and SEI which were detectible with both optical microscopy and WLI. Generally, surface wrinkling

171   increases electrode surface area, and here translated into mechanical strains applied to the SEI, which can

172   be quantified with WLI.

173

174   As WLI measurements through an optical window and electrolyte are not ideal, surface topographies

175   were measured with WLI in an *ex situ* manner, after electrochemistry was conducted in the primary

176   custom-made electrochemical cell (described above and schematically shown in Figure S1a). This was

177   accomplished by using separate samples, each with identical starting parameters. Specifically, each

178   sample underwent three CV formation cycles (cf. supporting information section S5) before the Si

179   electrode potential was brought to (and held at) the value of interest in the following way. Linear voltage

180   sweeps at a rate of 0.1 mV/s brought the Si electrode potential to the value of interest, then, a 12-hour

181   long-term potentiostatic polarization was conducted before the SEI deformed electrode was removed

182   from the cell. The electrodes extracted from the cell were cleaned with dimethyl carbonate (DMC) before

183   *ex situ* WLI characterization (see Methods for details).

184

185   ***Chemical and structural measurements of the SEI via spectroscopy and microscopy.*** *Ex situ* attenuated

186   total reflectance Fourier-transform infrared spectroscopy (ATR-FTIR) measurements were conducted to

187   characterize the vibrational spectra of electrodes over microscale surface areas. Moreover, in order to

188   characterize the electrode surface morphology, structure, and chemical composition at nanoscale

189   resolution, *ex situ* atomic force microscopy (AFM) based near-field Fourier transform infrared

190   nanospectroscopy (nano-FTIR) measurements were conducted;[34,35] a method recently used to probe

191   electrochemical surfaces[36] and interfaces.[37,38] Both tools were enclosed within a N_2-filled glovebox, and

192   further technical details, including how nano-FTIR breaks the diffraction limit, can be found in the

193   Methods section.

194

195   ***Strain evolution of compliant Si electrodes on PDMS.*** Figure 2 presents *in situ* optical microscopy

196   images of the surface of the 'SEI deformed' electrode (PDMS substrate) during five CV cycles between

197   0.05 – 1.5 V at a sweep rate of 0.1 mV/s. As the Si electrode expanded upon lithiation, the compliance of

198   the PDMS substrate allowed in-plane expansion, ultimately resulting in the formation of a dense pattern

199   of irregular surface wrinkles. When the Si electrode was delithiated, the surface smooths out, and

200   wrinkles disappear, as the Si contracted back to its original shape and surface area.

201 The surface morphology changes appear to be consistently reproducible, although the position and shape

202 of individual wrinkles tended to vary with each CV cycle. Importantly, electrochemically induced

203 deformation of the Si electrode upon charging/discharging necessarily caused the SEI layer to stretch out

204 and contract to absorb associated mechanical stress. While the data displayed in Figure 2b is certainly

205 convincing that these phenomena are occurring, it is only a qualitative measure, and cannot capture the

206 three-dimensional topography that is required for a full evaluation and quantification of the strain induced

207 in the SEI. Therefore, we then turned to WLI for quantitative measurements of strain.

208

Figure 2. Surface morphology evolution of the 'SEI deformed' (PDMS substrate) electrode captured by in

209

210 Quantitative biaxial strain values induced in the SEI on the deformed electrode on the PDMS substrate

211 were obtained by *ex situ* WLI measurements, as described previously in this work. Data collected after

212 three formation cycles is presented in Figure 3. All topography images share the same color scale bar (0

213 – 6 μm), with the minimum data point being zero (Figure 3a). Using 3D topography analysis software

214 (Gwyddion), actual surface area-to-projection area ratios at each potential value were calculated. Biaxial

215   SEI strain values calculated with respect to the delithiated state at 1.5 V, are presented in Figure 3b. The

216   details of the calculation procedure are described in supporting information section S2.
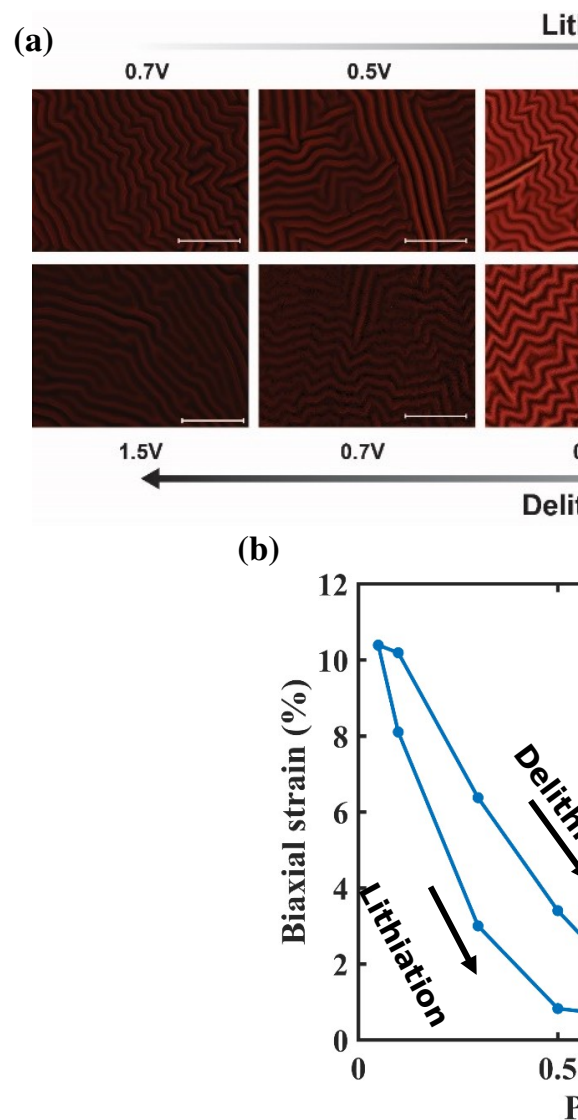

Figure 3. (a) 3D WLI images of ex situ Si electrodes on PDMS at different potentials after three SEI formation cycles. The inset sc

217

218   As shown in Figure 3b, the SEI layer experienced a maximum biaxial strain of about 10%, at the lower

219   cutoff potential of 0.05 V. Here, the observed maximum biaxial strain of ~10% is perhaps smaller than

220   what may be expected for a heavily lithiated Si anode – a material known for its dramatic volume

221 changes. However, as we will describe, this is actually reasonable. Recall that the Si thin-film was still

222 bonded via the PDMS layer to the Ni/Ti current collector film and fused silica substrate, which did not

223 undergo volume change during electrochemical cycling. While the overall stiffness of the electrode

224 certainly allowed deformation, the current collector and PDMS substrate still constrained the in-plane

225 deformation of the Si thin-film to some extent. In consequence, the Si in-plane expansion was limited to

226 ~10%, and the dominant expansion occurred in the out-of-plane direction. Nevertheless, the magnitude

227 of strain realized is easily still sufficient to explore how mechanical deformation of the SEI influences

228 passivation stability. In fact, a previously published study of the SEI layer formed from chemical

229 reactions between a lithium thin film and EC-based electrolyte showed the formation of multiple cracks at

230 as low as ~3% strain, and major failure at ~5.6% strain,[39] about half of what we observe. Thus, the

231 maximum strain observed in this study was nearly twice that of what is known to induce severe explicit

232 mechanical failure of the SEI.

233 Before moving onto discussing parasitic current measurements and evolution, we mention one other

234 observation from the data displayed in Figure 3b. That is, during the reverse delithiation sweep,

235 hysteresis in the biaxial strain is clearly observed between 0.05 – 0.2 V. A similar hysteresis-like

236 dependence during Si lithiation and delithiation has also been reported for Si expansion ratios vs.

237 potential.[40]

238

239 ***Differences in parasitic current values and evolution observed in the deformed and undeformed SEIs.***

240 Figure 4 presents the results of long-term potentiostatic polarization tests, preceded by linear voltage

241 sweeps, which enable direct measurements of the so-called parasitic current density associated with

242 electrolyte reduction. For each linear voltage sweep, which appears almost step-like in Figure 4a, we

243 observe a corresponding-in-time spike in current density due to a combination of lithiation/delithiation

244 reactions, electrolyte reduction, and SEI (re)formation. The magnitude of these current spikes is similar in

245 both the deformed and undeformed SEI cases. This similarity arises because, during the linear sweeps,

246 current is dominated by charge transfer associated with the lithiation/delithiation reaction of the finite

247 amount of Si in the congruently sized thin-film electrodes. However, as will be shown in the following

248 paragraphs, scientifically meaningful current density discrepancies between the deformed and

249 undeformed cases can be found at the temporal limits of the 12-hour-long potentiostatic polarizations,

250 where steady state current densities, called "parasitic current density," are realized. These limiting

251 parasitic current densities are irreversible, originate entirely from electrolyte reduction, and would vanish

252 if the electrode surface was fully passivated.

Figure 4. (a) Representative plots of the applied potential (dashed lines) and resulting current evolution (solid lines) from the parasi

254 The parasitic current density values for both the deformed and undeformed SEI electrodes are presented

255 in Figure 4b, and they never dropped to zero. This indicates that neither the undeformed or deformed SEI

256 fully passivates the Si electrode. For the undeformed SEI case, the parasitic current density can be

257 attributed to the inherent non-passivating behavior of the SEI layer on Si in carbonate-based electrolytes

258 (via physicochemical imperfections).[16] On the other hand, the SEI on the deformed Si electrode

259 experienced current density contributions originating from both the inherent non-passivating behavior,

260 and mechanically induced strain. Thus, the difference in parasitic current densities (Figure 4c) can be

261 attributed to effects linked with mechanical stretching of the SEI. Before discussing further observations

262 and implications related to the parasitic current density values and evolution, we provide additional

263 details on the presented data.

264

265 First, we note that each parasitic current density value (current per area) reported is (i) a mean value

266 calculated from three separate measurements and (ii) is area corrected in a self-consistent way utilizing

267 the strain data presented in Figure 3b, and methods described in supporting information section S2, so

268 that surface area increases via in-plane expansion of the Si electrode in the SEI deformed case are

269 accounted for. Second, while not displayed in Figure 4b, both electrodes showed substantially higher

270 parasitic current densities (and standard deviations) at potentials > 0.3 V during the lithiation sweep and

271 potentials > 0.7 V during the delithiation sweep (see supporting information section S3 and supporting

272 Figure S2). In principle, such behavior during the first cycle could be explained by electrolyte reduction

273 and formation of a not-fully-passivating SEI on the electrode surface. However, such behavior persists

274 during subsequent cycles, indicating the so-called 'SEI breathing' effect[16] is at play, where during the

275 delithiation process some critical SEI components – such as lithium ethylene dicarbonate (LiEDC) and

276 $LiPF_6$ (decomposition products which form during the prior lithiation process) – dissolve into the

277 electrolyte. The dissolution of these species during delithiation compromises the passivity of the film in

278   such a way that high parasitic currents are realized both at higher potentials during the anodic delithiation

279   sweep, and during the subsequent cathodic sweep for lithiation (until the SEI is fully reformed). Because

280   large parasitic currents in these potential windows are primarily governed by the SEI breathing effect, and

281   the contribution from mechanical effects is expected to be minimal, we therefore focus our attention in

282   this study on the subset of data decidedly outside these potential windows: potentials $\leq$ 0.3 V during the

283   lithiation sweep and potentials $\leq$ 0.7 V during delithiation sweep (Figure 4b and c).

284

285   When the electrode potential dropped below the lithiation potential (~0.3 V), the SEI became comparably

286   passivating, and the parasitic current density significantly decreases in comparison to 0.7 V. From that

287   point on, the parasitic current density gradually increases (Figure 4b) as the electrode potential decreased

288   and Si expanded (lithiation process) reaching a maximum value of ~0.25 $\mu A/cm^2$. During the delithiation

289   process the parasitic current density decreased as the potential increased and Si contracted. As shown in

290   Figure 4b, this trend was consistently observed for both the deformed and undeformed SEI electrodes.

291   Generally, this behavior is expected because the rate of the electrolyte reduction increases as the electrode

292   potential decreases.[41] However, the deformed SEI electrode clearly had higher parasitic current densities

293   in comparison to the undeformed SEI electrode, as highlighted in Figure 4c. It should be emphasized

294   again here that the only difference between the two Si electrodes was the presence or absence of

295   mechanical deformation of the SEI. As discussed previously, the 12-hour-long potentiostatic hold should

296   be sufficiently long to allow for SEI reformation in the event of explicit SEI cracking or delamination.

297   Thus, the observed increased parasitic current densities for the deformed SEI electrode must in some way

298   be associated with the static mechanical strain realized within the SEI (presented in Figure 3), which

299   apparently aggravates the already inherent non-passivating behavior. The deformed SEI electrode shows

300   parasitic current densities 10 – 25% higher than the undeformed SEI electrode (about ~ 0.02 – 0.06

301    $\mu A/cm^2$ above the undeformed SEI electrode in absolute current density terms).   The persistence of

302 parasitic current density during both the first and second cycles suggests that the mechanical effect

303 continues to influence surface passivation regardless of deformation history.

304

305 ***Nano- and ATR-FTIR spectroscopies imply EMC and decomposition products are trapped deep in the***

306 ***SEI near the Si surface.*** FTIR measurements were conducted to gain further insight into how

307 mechanical strain in the SEI could alter the film structure and chemical composition. Figure 5 presents *ex*

308 *situ* ATR-FTIR spectra of the 'deformed and undeformed SEI' electrodes after the parasitic current

309 measurements (delithiated to 1.5 V). The peak at 1010 cm^{-1} (marked by a black asterisk) is attributed to

310 the underlying PDMS substrate. The peaks that are commonly observed in the spectra of both the

311 'deformed and undeformed SEI' electrodes correspond to dried electrolyte i.e., $LiPF_6$ and EC, and

312 polyethylene glycol oligomers and P–F, P–O–F containing compounds from $LiPF_6$ decomposition. The

313 spectra are in strong agreement with those previously reported by Hasa *et al.*[16] which characterized the

314 SEI on Si thin-film electrodes using the same electrolyte compositions. Notably, there is an absence of

315 peaks corresponding to LiEDC (typically distinguishable by IR band at 1652cm^{-1}) in the spectra. This is

316 because the measurements were performed at a delithiated state (1.5 V vs. Li/Li$^+$) and LiEDC would have

317 dissolved, according to the 'SEI breathing' effect reported by Hasa *et al.*[16]

318

319 Interestingly, the FTIR spectrum of the 'deformed SEI' electrode displays IR bands at 1275, 1306, 1375,

320 and 1450 cm^{-1} (marked by red asterisks), which cannot be attributed to the underlying PDMS substrate

321 and are not seen in the 'undeformed SEI' electrode. Surprisingly, all these peaks match the IR signature

322 of EMC.[42] Peaks at 1375 and 1450 cm^{-1} can be assigned to -C-H bending modes in -CH$_3$, whereas those at

323 1275 and 1306 cm^{-1} can be assigned to C(O)-O stretching in EMC. The presence of EMC IR vibration

324 modes is unexpected because EMC is a highly volatile solvent that should evaporate quickly from the

325   electrolyte surface during the extensive drying process (see Methods section for details), as is found in the

326   'undeformed SEI' electrode. Therefore, the ATR-FTIR measurements may indicate that EMC was

327   entrapped in the SEI layer bulk upon mechanical deformation of the film. Another notable difference

328   between the two spectra is a shoulder at *ca.* 1170 cm^{-1} next to the C-O stretching mode of EC at 1200 cm^{-1}

329   (highlighted by a blue asterisk). This band becomes even more prominent in nano-FTIR spectra (Figure

330   6) and is assigned to EMC transesterification products.

331   Figure 6 presents *ex situ* AFM topography images and nano-FTIR spectra collected on the 'deformed

332   SEI' electrode at 1.5 V. The AFM image (Figure 6a) shows the SEI film morphology which is relatively

333   rough (RMS = 51.2 nm), inhomogeneous, and comprised of nanoscale particles and clusters ranging in

334   size from 1–100 nm in diameter. The colored circles identify locations where nano-FTIR measurements

335   were performed.

Figure 6. Ex situ ano-FTIR measurements of the 'deformed SEI' electrode (delithiated to 1.5 V). (a) AFM topography image show:

336

337 Figure 6b shows ATR- and nano-FTIR spectra (point #1) of the 'deformed SEI' electrode. The ATR and

338 nano-FTIR spectra show well-pronounced peaks around 1265 and 1306 cm^{-1}, which correspond to the

339 C(O)-O stretching modes in EMC. However, the -C-H bending modes in CH$_3$ (1375 and 1450 cm^{-1}) are

340 somewhat reduced in intensity with regard to the ATR-FTIR spectrum. Variations in EMC IR band

341 positions and intensity can be related to nanoconfinement of EMC. In fact, the nano-FTIR probe is more

342 sensitive to (i) local chemistry and structure of *ca.* 10 nm diameter probing region directly below the

343 AFM tip, (ii) molecular/dipole configurations due to local chemical environment, and (iii) localized

344 concentration of chemical species which otherwise is impossible to observe in the spatially averaged

345 ATR-FTIR spectrum. Nanoconfinement of liquids, or their nanoscopic interactions at an interface, are

346 known to significantly change the structural dynamics of hydrogen bonds. This phenomenon largely

347 affects the position and intensity of corresponding IR absorption bands, as demonstrated by ultrafast IR

348 spectroscopy on nanoscale-trapped water in reverse micelle structures.[43,44] In light of these facts, the

349 relatively weak CH_3 deformation bands (at 1375 and 1450 cm^{-1}) in the nano-FTIR spectra can be

350 attributed to the EMC nanoconfinement in the SEI.

351 Another distinguishing feature of the nano-FTIR spectra in comparison to the ATR-FTIR spectra is the

352 total absence of EC absorption bands; notably ring breathing modes at ~1195 and 1080 cm^{-1}. Recall that

353 the samples are not washed with DMC for ATR-FTIR measurements. Thus, the EC signal in the ATR-

354 FTIR spectra can be attributed to the residual dried electrolyte components on the sample surface. The

355 presence of EMC and absence of EC in the nano-FTIR spectra suggest that the mechanical stretching

356 alters the SEI structure to allow selective transport of EMC through it. The nano-FTIR spectra also show

357 a strong peak around 1180 cm^{-1} wavenumber, which is also visible as a shoulder in the ATR FTIR

358 spectrum of the 'deformed SEI' electrode. This IR peak corresponds to the C-O stretching of an ester

359 compound.[45] Previous studies using gas or liquid chromatography-mass spectrometry (GC or LC-MS)

360 revealed that thermal and electrochemical decomposition (transesterification) of EC/EMC solvents

361 generates electrolyte soluble species such as dimethyl-2,5-dioxahexane carboxylate (DMDOHC),

362 ethylmethyl-2, 5-dioxahexane dicarboxylate (EMDOHC), diethyl-2, 5-dioxahexane dicarboxylate

363 (DEDOHC) and other various oligomeric compounds.[46-48] The strong peak at 1180 cm^{-1} suggests the

364 formation and confinement of these soluble EMC decomposition products in the SEI layer on the

365 'deformed Si' electrode. Unfortunately, FTIR spectra of these chemical compounds are rarely reported

366 due to their solubility in the electrolyte. To the best of our knowledge, reference FTIR spectrum of

367 synthetic DEDOHC exhibits a dominant peak at ~1234 cm^{-1} in the 1000-1500 cm^{-1} wavenumber range.[49]

368 A contour plot of the ten-point linescan of nano-FTIR spectra (Figure 6c) shows significant variations

369 with location. To understand EMC and its transesterification reduction products confinement in the SEI

370 layer and potential correlation with the film structure, we monitor their spatial variance. The plot of AFM

371 cross-sectional topography and the corresponding nano-FTIR absorption intensity variations at 1180 and

372 1265 cm^{-1} which are representative of EMC and the transesterification product, respectively (Figure 6d.)

373 suggests that these compounds tend to be buried deep in the SEI film. This correlation can arise from two

374 reasons: (i) the total amount of IR backscattering is higher at lower topography due to higher electronic

375 conductivity of the underlying electrode, and/or (ii) the EMC and its transesterification products are

376 captured in sections of the SEI layer adjacent to the surface of the Si electrode. To evaluate and quantify

377 possible contributions to the nano-FTIR signal, variations of IR absorption at several wavenumbers and

378 their correlations with topography are examined (see supporting information S4 for details). We selected

379 a wavenumber (1210 cm^{-1}) where the absorption is the minimum, and two arbitrary wave numbers (1050

380 and 1350 cm^{-1}), which are not obvious IR peak locations relevant to EMC. It turns out that no clear

381 correlation exists between the absorption and topography for features at wavenumbers of 1050, 1210, and

382 1350 cm^{-1} (see Figure S3 in the supporting information). Thus, the clear inverse correlation between the

383 EMC and EMC transesterification product signals and the topography shown in Figure 6d does not

384 originate from the total amount of IR light back scattering. Rather, it is most likely that EMC and EMC

385 transesterification products are trapped deep in the SEI layer in the vicinity of the Si electrode surface.

386 ***Unearthing a passivation failure mechanism in statically strained SEIs on Si critical to calendar life.***

387 The results presented here provide direct evidence of the SEI layer failure mode upon mechanical

388 stretching of Si. Figure 7 shows a schematic representation of the suggested surface passivation failure

389 mechanism. As Si expands during lithiation, and stretches the SEI layer, the associated tensile strain leads

390 to loosening of local structure and morphology in the SEI film. This structural loosening opens up small

391 channels and voids in the film that allow EMC and/or EMC solvated Li$^+$ ions to penetrate. Once the Si

surface is reached, local EMC electroreduction is promoted. A likely means of EMC transport through these nano-channels of the stretched SEI is selective diffusion via strain-induced EMC-specific transport pathways. In fact, a similar phenomenon of selective transport of linear carbonates through an artificial SEI on Si has already been observed. In that case, the poly 1-pyrenemethyl methacrylate (PPy) artificial SEI selectively permitted transport of linear carbonates, and the resulting continuous side reactions prevented successful passivation.[50] All that said, for the present case, in order to confirm the exact EMC transport mechanism and details, and the nature of chemical mediators in the SEI layer, further research is required.

Upon delithiation, the silicon and SEI layer contract, capturing EMC diffusing from the electrolyte and soluble electrolyte decomposition products in it. The EMC entrapment and subsequent decomposition appear to happen in the small section of the SEI layer that is adjacent to the electrode surface, where we believe the electrode passivation takes place. Mechanical and chemical integrity of this active part of the SEI is essential for the long-term interfacial stability of the Si electrode. The emergence of these parasitic currents imply consumption of cyclable lithium, electrolyte drying, and possibly gas formation, all while the cell is at rest. Thus, it is highly relevant to the calendar life of Si anode batteries utilizing organic carbonate electrolytes. Our findings reveal that the state of mechanical strain experienced by the SEI has a significant influence on the inherent non-passivating behavior.

It should be emphasized again that this uncovered failure mechanism is originating from the static strain applied in the SEI, which worsens the inherent non-passivating behavior of Si. It is not necessarily linked with the SEI layer catastrophic breakdown upon Si particle decrepitation and composite electrode delamination. Thus, the mechanism studied in this work is more relevant to the observed limitations in the calendar life of Si electrodes in carbonate electrolytes rather than cycle performance. The observed failure mechanism of the SEI layer upon mechanical deformation aggravates the interfacial instability of the silicon electrode and should be considered in future mitigation strategies.
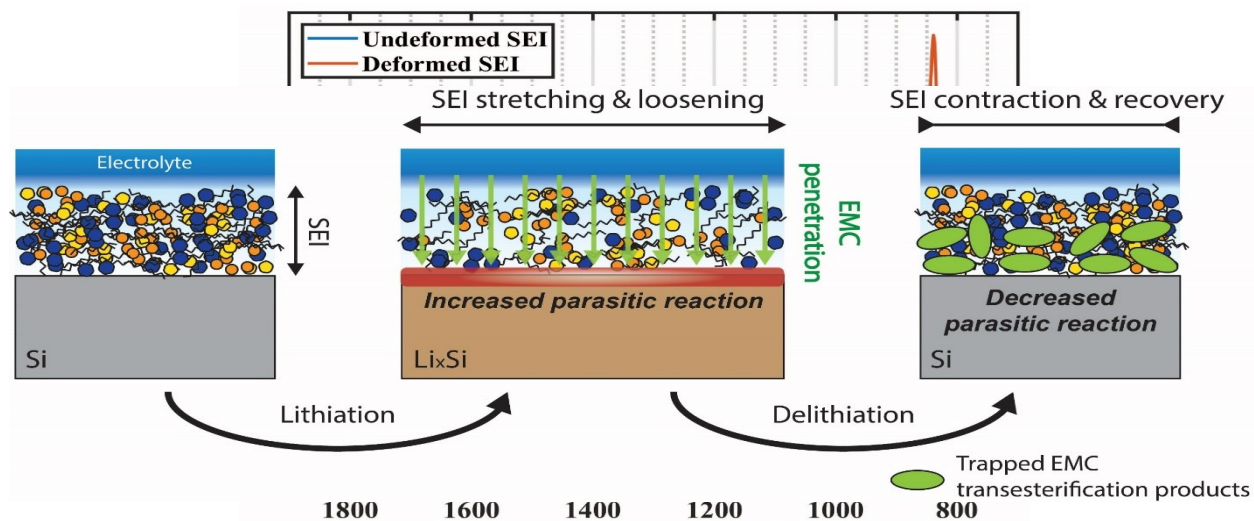
416

Figure 7. Schematic representation of the suggested passivation failure mechanism arisen from the mechanical deformation of the SEI. Lithiation-induced mechanical stretching allows selective EMC penetration through the SEI followed by electroreduction at the Si surface. Subsequent delithiation retains the structural integrity of the SEI layer and confines EMC and its transesterification products in the SEI.

CONCLUSIONS

A comparative experimental approach has been designed and conducted to investigate the impact that static mechanical deformation of the SEI on Si has on surface passivation stability. This is achieved by using samples with two types of substrates – polymeric and ceramic – in which only one is compliant (the polymeric substrate) and the corresponding SEI undergoes mechanical deformation, while the other does not. A comparison of the electrochemical performance of the two types of samples unambiguously reveals the effect and magnitude of the mechanical stress on the passivation behavior of the Si electrode. The mechanical in-plane strain of ~10% applied in the SEI appears to increase the interfacial parasitic current by 10 – 25%. Because the strain experienced by the SEI in realistic Si composite anode systems is expected to be much higher than those controllably induced here, this static mechanical effect

428 uncovered in this work should have substantial influence on parasitic side reactions realized during

429 calendar aging. *Ex situ* ATR- and nano-FTIR measurements reveal that mechanical stretching leads to

430 nanoconfinement of EMC and its transesterification products from the EMC decomposition reactions

431 within the SEI, close to the surface of the Si electrode. These findings strongly suggest that tensile strain

432 loosens the structure of the SEI, allowing selective EMC penetration, which ultimately increases the rate

433 of parasitic reactions. The mechanical effects and failure mechanism uncovered in this work directly

434 affects calendar life of Si-anode LIBs, and provides guiding insight into what future engineering efforts

435 should attempt to address when aiming to optimize passivation stability Si anode SEIs experiencing static

436 mechanical deformation when the cell is at rest.

437

438 **METHODS**

439 ***Plasma treatments.*** Oxygen plasma treatments were conducted on both the soft and rigid substrates prior

440 to sputtering electrode materials. The oxygen plasma treatments were conducted via a Yield Engineering

441 Systems G500. The duration was 60 seconds at 200 W power to remove common surface contaminants

442 and, in turn, promote strong bonding/adhesion between the cleaned surface and any subsequent materials

443 deposition.

444

445 ***Sputter depositions of current collectors and electrodes.*** Ti/Ni/Si layers were deposited onto both the

446 soft and rigid substrates post oxygen plasma treatment. Samples were immediately loaded into a

447 sputtering machine (K.J. Lesker) for thin-film Si electrode deposition. The chamber was first evacuated

448 below 1.0×10^{-5} Torr. Then, Ar gas was injected to maintain a processing pressure of $\sim 2 \times 10^{-3}$ Torr. A

449 titanium adhesion layer (~5 nm) was sputtered first, followed by deposition of a ~40 nm thick layer of

450 nickel. The nickel thin-film functioned as the current collector. Finally, a thin ~50 nm Si film was

451   deposited atop the nickel current collector. All sputtering source targets (K. J. Lesker) used in this study

452   had 75 mm diameter and purity >99.99% (K.J. Lesker).

453

454   ***Electrochemical cell details.*** Approximately 2 mL of electrolyte composed of 1.2 M lithium

455   hexafluorophosphate ($LiPF_6$) in ethylene carbonate (EC) and ethyl methyl carbonate (EMC) with a 3:7

456   weight ratio was used. The cell was sealed using a Kalrez o-ring and tightened with screws. Cell

457   assembly was performed in an Ar-filled glove box (Nexus Vacuum Atmospheres Co.) with O_2/H_2O levels

458   <0.1 ppm.

459

460   ***White light interferometry.*** Electrodes were removed from cells and cleaned with DMC before being

461   transported to a Zygo NewView 6000 optical profilometer in an air-tight vessel filled with Ar, where

462   three-dimensional (3D) surface topography of the Si electrodes were measured, *ex situ*. The WLI captured

463   ~263 × 350 μm images of the projected area with a resolution of 640 × 480 pixels. The actual surface

464   area-to-projection area ratio was calculated using a 3D topography data analysis software (Gwyddion).

465

466   ***ATR-FTIR.*** ATR-FTIR was conducted in a nitrogen-filled glovebox using a Shimadzu IRTracer-

467   100 system equipped with a Ge crystal. Spectra were collected with 4 cm^{-1} resolution over a 700

468   – 2000 cm^{-1} wavenumber range. Prior to the ATR-FTIR measurements, the samples were dried

469   (without any washing process) in an Ar-filled glovebox for *ca.* 24 hours and then another hour in

470   the glovebox antechamber under *ca.* 1 Torr vacuum to completely remove residual electrolyte

471   solvents. Samples were then transferred to the N_2-filled glovebox using an air-tight vessel filled

472   with Ar.

473

474   ***Nano-FTIR.*** We used a commercial NeaSNOM system (Neaspec) enclosed within a N_2-filled

475   glovebox. Notably, nano-FTIR breaks the diffraction limit and enables nanoscale infrared

476   spectroscopy and imaging. This is accomplished by first collecting the IR light backscattered

477   from the sample surface/probe-tip junction. Then, light attributable to near-field scattering

478   processes from nanoscopic volumes at and around the probe-tip end is extracted from the

479   backscattered signal with a combination of asymmetric Michelson interferometry and lock-in

480   demodulation at integer values of the probe's tapping frequency (~250 kHz). Near-field signals

481   are further isolated by normalization to spectrally flat references spectra, e.g., gold or silicon. In

482   this work, we report the second harmonic of the imaginary part of the complex spectrum

483   normalized to Si as nano-FTIR absorption. Additionally, probes used were platinum-iridium

484   coated "nano-FTIR" probes (Neaspec) which were driven to oscillate with a tapping amplitude

485   of ~63 nm during data acquisition. A broadband IR laser with a wavelength range between

486   ~1000 – 1500 cm^{-1} was used, and all spectra were collected with 8 cm^{-1} resolution. The samples

487   prepared and transferred in a similar manner as described above for ATR-FTIR measurements.

488

489

490

491

492

493

494

ASSOCIATED CONTENT

Supporting Information

The Supporting Information is available free of charge at [[LINK TO BE INSERTED BY ACS Nano]]

Illustrations of the custom cells used in this study, SEI layer biaxial strain calculations, parasitic current density vs. potential, analysis of nano-FTIR spectra vs. SEI layer topography, and initial cyclic voltammograms of Si electrodes

AUTHOR INFORMATION

Corresponding Author

*Robert Kostecki

Authors

‡Insun Yoon

‡Jonathan M. Larson

510

Author Contributions

512 ‡I.Y. and J.M.L. contributed equally to this work.

513

514 **Notes**

515 The authors declare no competing financial interest.

516

523

524 **REFERENCES**

525 (1) Boukamp, B. A.; Lesh, G. C.; Huggins, R. A. All-solid Lithium Electrodes with Mixed-conductor Matrix.
526 *J. Electrochem. Soc.* **1981**, *128*, 725–729.

527 (2) Liang, B.; Liu, Y.; Xu, Y. Silicon-Based Materials as High Capacity Anodes for next Generation Lithium
528 Ion Batteries. *J. Power Sources* **2014**, *267*, 469–490.

529 (3) Kasavajjula, U.; Wang, C.; Appleby, A. J. Nano-and Bulk-Silicon-Based Insertion Anodes for Lithium-
530 Ion Secondary Cells. *J. Power Sources* **2007**, *163*, 1003–1039.

531 (4) Beaulieu, L. Y.; Eberman, K. W.; Turner, R. L.; Krause, L. J.; Dahn, J. R. Colossal Reversible Volume
532 Changes in Lithium Alloys. *Electrochem. Solid-State Lett.* **2001**, *4*, A137.

(533) Xiao, X.; Liu, P.; Verbrugge, M. W.; Haftbaradaran, H.; Gao, H. Improved Cycling Stability of Silicon Thin Film Electrodes through Patterning for High Energy Density Lithium Batteries. *J. Power Sources* **2011**, *196*, 1409–1416.

(536) Wu, H.; Chan, G.; Choi, J. W.; Ryu, I.; Yao, Y.; McDowell, M. T.; Lee, S. W.; Jackson, A.; Yang, Y.; Hu, L. Stable Cycling of Double-Walled Silicon Nanotube Battery Anodes through Solid–Electrolyte Interphase Control. *Nat. Nanotechnol.* **2012**, *7*, 310–315.

(539) Zhang, X.; Wang, D.; Qiu, X.; Ma, Y.; Kong, D.; Müllen, K.; Li, X.; Zhi, L. Stable High-Capacity and High-Rate Silicon-Based Lithium Battery Anodes upon Two-Dimensional Covalent Encapsulation. *Nat. Commun.* **2020**, *11*, 1–9.

(542) Yao, Y.; McDowell, M. T.; Ryu, I.; Wu, H.; Liu, N.; Hu, L.; Nix, W. D.; Cui, Y. Interconnected Silicon Hollow Nanospheres for Lithium-Ion Battery Anodes with Long Cycle Life. *Nano Lett.* **2011**, *11*, 2949–2954.

(545) He, T.; Feng, J.; Zhang, Y.; Zu, L.; Wang, G.; Yu, Y.; Yang, J. Stress-relieved Nanowires by Silicon Substitution for High-capacity and Stable Lithium Storage. *Adv. Energy Mater.* **2018**, *8*, 1702805.

(547) Szczech, J. R.; Jin, S. Nanostructured Silicon for High Capacity Lithium Battery Anodes. *Energy Environ. Sci.* **2011**, *4*, 56–72.

(549) Veith, G. M.; Doucet, M.; Sacci, R. L.; Vacaliuc, B.; Baldwin, J. K.; Browning, J. F. Determination of the Solid Electrolyte Interphase Structure Grown on a Silicon Electrode Using a Fluoroethylene Carbonate Additive. *Sci. Rep.* **2017**, *7*, 1–15.

(552) Lu, W.; Zhang, L.; Qin, Y.; Jansen, A. Calendar and Cycle Life of Lithium-Ion Batteries Containing Silicon Monoxide Anode. *J. Electrochem. Soc.* **2018**, *165*, A2179.

(554) Peled, E. The Electrochemical Behavior of Alkali and Alkaline Earth Metals in Nonaqueous Battery Systems—the Solid Electrolyte Interphase Model. *J. Electrochem. Soc.* **1979**, *126*, 2047.

(556) Balbuena, P. B.; Wang, Y. X.; *Lithium-Ion Batteries: Solid-Electrolyte Interphase*, Imperial College Press: London, 2004.

(558) Peled, E.; Menkin, S. SEI: Past, Present and Future. *J. Electrochem. Soc.* **2017**, *164*, A1703.

(559) Hasa, I.; Haregewoin, A. M.; Zhang, L.; Tsai, W.-Y.; Guo, J.; Veith, G. M.; Ross, P. N.; Kostecki, R. Electrochemical Reactivity and Passivation of Silicon Thin-Film Electrodes in Organic Carbonate Electrolytes. *ACS Appl. Mater. Interfaces* **2020**, *12*, 40879–40890.

(562) Kalaga, K.; Rodrigues, M.-T. F.; Trask, S. E.; Shkrob, I. A.; Abraham, D. P. Calendar-Life versus Cycle-Life Aging of Lithium-Ion Cells with Silicon-Graphite Composite Electrodes. *Electrochim. Acta* **2018**, *280*, 221–228.

(565) Guo, K.; Kumar, R.; Xiao, X.; Sheldon, B. W.; Gao, H. Failure Progression in the Solid Electrolyte Interphase (SEI) on Silicon Electrodes. *Nano Energy* **2020**, *68*, 104257.

(567) Kumar, R.; Tokranov, A.; Sheldon, B. W.; Xiao, X.; Huang, Z.; Li, C.; Mueller, T. In Situ and Operando Investigations of Failure Mechanisms of the Solid Electrolyte Interphase on Silicon Electrodes. *ACS Energy Lett.* **2016**, *1*, 689–697.

(570) Kamikawa, Y.; Amezawa, K.; Terada, K. Elastic–Plastic Deformation of a Solid Electrolyte Interface Formed by Reduction of Fluoroethylene Carbonate: A Nanoindentation and Finite Element Analysis Study. *J. Phys. Chem. C* **2020**, *124*, 22488–22495.

(571) Tanaka, M.; Hooper, J. B.; Bedrov, D. Role of Plasticity in Mechanical Failure of Solid Electrolyte Interphases on Nanostructured Silicon Electrode: Insight from Continuum Level Modeling. *ACS Appl. Energy Mater.* **2018**, *1*, 1858–1863.

(572) Single, F.; Horstmann, B.; Latz, A. Revealing SEI Morphology: In-Depth Analysis of a Modeling Approach. *J. Electrochem. Soc.* **2017**, *164*, E3132.

(573) Single, F.; Horstmann, B.; Latz, A. Dynamics and Morphology of Solid Electrolyte Interphase (SEI). *Phys. Chem. Chem. Phys.* **2016**, *18*, 17810–17814.

(574) Tokranov, A.; Kumar, R.; Li, C.; Minne, S.; Xiao, X.; Sheldon, B. W. Control and Optimization of the Electrochemical and Mechanical Properties of the Solid Electrolyte Interphase on Silicon Electrodes in Lithium Ion Batteries. *Adv. Energy Mater.* **2016**, *6*, 1502302.

(575) Yoon, I.; Jurng, S.; Abraham, D. P.; Lucht, B. L.; Guduru, P. R. In Situ Measurement of the Plane-Strain Modulus of the Solid Electrolyte Interphase on Lithium-Metal Anodes in Ionic Liquid Electrolytes. *Nano Lett.* **2018**, *18*, 5752–5759.

(576) Cook, R. F.; Pharr, G. M. Direct Observation and Analysis of Indentation Cracking in Glasses and Ceramics. *J. Am. Ceram. Soc.* **1990**, *73*, 787–817.

(577) Sethuraman, V. A.; Chon, M. J.; Shimshak, M.; Srinivasan, V.; Guduru, P. R. In Situ Measurements of Stress Evolution in Silicon Thin Films during Electrochemical Lithiation and Delithiation. *J. Power Sources* **2010**, *195*, 5062–5066.

(578) Johnston, I. D.; McCluskey, D. K.; Tan, C. K. L.; Tracey, M. C. Mechanical Characterization of Bulk Sylgard 184 for Microfluidics and Microengineering. *J. Micromech. Microeng.* **2014**, *24*, 35017.

(579) Yu, C.; Li, X.; Ma, T.; Rong, J.; Zhang, R.; Shaffer, J.; An, Y.; Liu, Q.; Wei, B.; Jiang, H. Silicon Thin Films as Anodes for High-performance Lithium-ion Batteries with Effective Stress Relaxation. *Adv. Energy Mater.* **2012**, *2*, 68–73.

(580) Bowden, N.; Brittain, S.; Evans, A. G.; Hutchinson, J. W.; Whitesides, G. M. Spontaneous Formation of Ordered Structures in Thin Films of Metals Supported on an Elastomeric Polymer. *Nature* **1998**, *393*, 146–149.

(581) Huang, T.; Song, J.; He, S.; Li, T.; Li, X.-M.; He, T. Enabling Sustainable Green Close-Loop Membrane Lithium Extraction by Acid and Solvent Resistant Poly (Ether Ether Ketone) Membrane. *J. Memb. Sci.* **2019**, *589*, 117273.

(582) Tan, C.; Daemi, S. R.; Taiwo, O. O.; Heenan, T. M. M.; Brett, D. J. L.; Shearing, P. R. Evolution of Electrochemical Cell Designs for In-Situ and Operando 3D Characterization. *Materials* **2018**, *11*, 2157.

(583) Schulze, M. C.; Rodrigues, M.-T. F.; McBrayer, J. D.; Abraham, D. P.; Apblett, C. A.; Bloom, I.; Chen, Z.; Colclasure, A. M.; Dunlop, A. R.; Fang, C. Critical Evaluation of Potentiostatic Holds as Accelerated Predictors of Capacity Fade during Calendar Aging. *J. Electrochem. Soc.* **2022**, *169*, 50531.

(607) Chen, X.; Hu, D.; Mescall, R.; You, G.; Basov, D. N.; Dai, Q.; Liu, M. Modern Scattering-type Scanning Near-field Optical Microscopy for Advanced Material Research. *Adv. Mater.* **2019**, *31*, 1804774.

(608) Huth, F. Nano-FTIR - Nanoscale Infrared Near-Field Spectroscopy. PhD, Euskal Herriko Unibertsitatea-Universidad del Pais Vasco, Spain, January 27, 2015.

(611)

(612) Dopilka, A.; Gu, Y.; Larson, J. M.; Zorba, V.; Kostecki, R. Nano-FTIR Spectroscopy of the Solid Electrolyte Interphase Layer on a Thin-Film Silicon Li-Ion Anode. *ACS Appl. Mater. Interfaces* **2023**, *15*, 6755-6767.

(615) Lu, Y.-H.; Larson, J. M.; Baskin, A.; Zhao, X.; Ashby, P. D.; Prendergast, D.; Bechtel, H. A.; Kostecki, R.; Salmeron, M. Infrared Nanospectroscopy at the Graphene–Electrolyte Interface. *Nano Lett.* **2019**, *19*, 5388–5393.

(618) He, X.; Larson, J. M.; Bechtel, H. A.; Kostecki, R. In Situ Infrared Nanospectroscopy of the Local Processes at the Li/Polymer Electrolyte Interface. *Nat. Commun.* **2022**, *13*, 1398.

(620) Yoon, I.; Jurng, S.; Abraham, D. P.; Lucht, B. L.; Guduru, P. R. Measurement of Mechanical and Fracture Properties of Solid Electrolyte Interphase on Lithium Metal Anodes in Lithium Ion Batteries. *Energy Storage Mater.* **2020**, *25*, 296-304.

(623) Yoon, I.; Abraham, D. P.; Lucht, B. L.; Bower, A. F.; Guduru, P. R. In Situ Measurement of Solid Electrolyte Interphase Evolution on Silicon Anodes Using Atomic Force Microscopy. *Adv. Energy Mater.* **2016**, *6*, 1600099.

(626) Xu, K. Nonaqueous Liquid Electrolytes for Lithium-Based Rechargeable Batteries. *Chem. Rev.* **2004**, *104*, 4303–4418.

(628) Pekarek, R. T.; Affolter, A.; Baranowski, L. L.; Coyle, J.; Hou, T.; Sivonxay, E.; Smith, B. A.; McAuliffe, R. D.; Persson, K. A.; Key, B. Intrinsic Chemical Reactivity of Solid-Electrolyte Interphase Components in Silicon–Lithium Alloy Anode Batteries Probed by FTIR Spectroscopy. *J. Mater. Chem. A* **2020**, *8*, 7897–7906.

(632) Fayer, M. D.; Levinger, N. E. Analysis of Water in Confined Geometries and at Interfaces. *Annu. Rev. Anal. Chem.* **2010**, *3*, 89–107.

(634) Fayer, M. D. Dynamics of Water Interacting with Interfaces, Molecules, and Ions. *Acc. Chem. Res.* **2012**, *45*, 3–14.

(636) Socrates, G.; *Infrared and Raman Characteristic Group Frequencies: Tables and Charts*, 3; John Wiley & Sons: West Sussex, 2004.

(638) Sloop, S. E.; Kerr, J. B.; Kinoshita, K. The Role of Li-Ion Battery Electrolyte Reactivity in Performance Decline and Self-Discharge. *J. Power Sources* **2003**, *119*, 330–337.

(640) Henschel, J.; Peschel, C.; Klein, S.; Horsthemke, F.; Winter, M.; Nowak, S. Clarification of Decomposition Pathways in a State-of-the-art Lithium Ion Battery Electrolyte through 13C-labeling of Electrolyte Components. *Angew. Chem.* **2020**, *132*, 6184–6193.

(643) Petibon, R.; Xia, J.; Burns, J. C.; Dahn, J. R. Study of the Consumption of Vinylene Carbonate in Li [Ni0. 33Mn0. 33Co0. 33] O2/Graphite Pouch Cells. *J. Electrochem. Soc.* **2014**, *161*, A1618.

(644) Shi, F.; Zhao, H.; Liu, G.; Ross, P. N.; Somorjai, G. A.; Komvopoulos, K. Identification of Diethyl 2, 5-Dioxahexane Dicarboxylate and Polyethylene Carbonate as Decomposition Products of Ethylene Carbonate Based Electrolytes by Fourier Transform Infrared Spectroscopy. *J. Phys. Chem. C* **2014**, *118*, 14732–14738.

(645) Haregewoin, A. M.; Terborg, L.; Zhang, L.; Jurng, S.; Lucht, B. L.; Guo, J.; Ross, P. N.; Kostecki, R. The Electrochemical Behavior of Poly 1-Pyrenemethyl Methacrylate Binder and Its Effect on the Interfacial Chemistry of a Silicon Electrode. *J. Power Sources* **2018**, *376*, 152–160.